

# Trajectory Optimization of Robots With Regenerative Drive Systems: Numerical and Experimental Results

Poya Khalaf<sup>ID</sup> and Hanz Richter<sup>ID</sup>

**Abstract**—In this paper, we investigate energy-optimal control of robots with ultracapacitor-based regenerative drive systems. Based on a previously introduced framework, a fairly generic model is considered for the robot and the drive system. An optimal control problem is formulated to find point-to-point trajectories maximizing the amount of energy regenerated and stored in the capacitor. The optimization problem, its numerical solution, and an experimental evaluation are demonstrated using a PUMA manipulator with custom regenerative drives. Power flows, stored regenerative energy, and efficiency are evaluated. Tracking of optimal trajectories is enforced on the robot using a standard robust passivity based control approach. Experimental results show that when following optimal trajectories, a reduction of about 10–22% in energy consumption can be achieved for the conditions of the study, relative to the nonregenerative case.

**Index Terms**—Biomedical computing, mathematical programming, medical robotics, motion planning, optimal control.

## I. INTRODUCTION

ENERGY regeneration technologies have gained much attention due to their potential to reduce the energy consumption of modern engineering systems. Lower energy consumption allows devices to work for longer periods of time with lower operational costs. These factors are crucial in the design of systems, such as electric and hybrid vehicles [1], powered prostheses [2] and exoskeletons [3], autonomous spacecraft [4], etc. The concept of energy regeneration is understood to be the process of recovering energy that would be otherwise dissipated, and redistributing or storing it for later use. The framework proposed in [5] allows energy optimization and motion controller designs to be conducted separately, by introducing a virtual controller and capacitor voltage feedback.

This paper is focused on the application of regenerative technologies to robotic systems. Incorporating regenerative design

Manuscript received December 12, 2018; revised April 29, 2019; accepted June 6, 2019. Date of publication July 12, 2019; date of current version April 2, 2020. This work was supported by the National Science Foundation under Grant 1344954 and Grant 1536035. This paper was recommended for publication by Associate Editor Quang-Cuong Pham and Editor Eiichi Yoshida upon evaluation of the reviewers' comments. (*Corresponding author: Hanz Richter*)

The authors are with the Department of Mechanical Engineering, Cleveland State University, Cleveland, OH 44122 USA (e-mail: p.khalaf@csuohio.edu; h.richter@csuohio.edu).

This paper has supplementary downloadable material available at <http://ieeexplore.ieee.org>, provided by the authors. The material consists of videos showing the PUMA 500 robot following optimized trajectories for the three studied cases. In addition, the MATLAB code for solving the trajectory optimization problem for the PUMA 500 robot is provided. The size of the video is 1.7 MB. Contact the corresponding author, h.richter@csuohio.edu

Color versions of one or more of the figures in this paper are available online at <http://ieeexplore.ieee.org>.

Digital Object Identifier 10.1109/TRO.2019.2923920

features is justified when a significant potential for energy recovery exists. Examples include fast-moving, multijoint industrial and mobile robots, and powered prostheses and powered exoskeletons. Excess energy can be stored from the robot joints while decelerating and reused when the robot joints are accelerating, thus, reducing the overall energy consumption. For an industrial manufacturing line with many robotic systems this can lead to a significant reduction in electric power costs. For powered prostheses and exoskeletons, energy regeneration can increase operating times, making them more practical for daily use.

In addition, robots with regenerative drive systems offer unique opportunities for joint-to-joint mechanical energy redistribution by electrical means. Strictly speaking, energy transfer among joints may naturally occur in robotic manipulators via inertial coupling. However, this kind of indirect energy transfer is governed by the structure, mass properties, and joint trajectories of the robot. In many cases, these factors are predefined and the joint-to-joint energy flow cannot be managed or controlled. For example, the structure of a Cartesian robot prevents any energy flow between joints due to the absence of coupling. Bidirectional power (4-quadrant) drive electronics offers the opportunity to configure pathways for joint-to-joint energy transfer and management. Excess energy regenerated from a joint that decelerates can be conveyed to another joint that is accelerating and demanding energy. In a regenerative Cartesian robot, this effectively enables energy transfer between joints. Such capabilities can lead to significant reduction in the energy consumption of the overall robot.

We consider regenerative drive systems that use capacitive means for storing energy. The development of electrochemical double layer capacitors, so-called ultracapacitors or supercapacitors, in the past decade have enabled efficient means of storing and reusing energy [6]. Unlike batteries, ultracapacitors can be charged and discharged at high rates without damage, and have considerably high power densities [7]. Being lightweight, inexpensive, and durable are other properties of ultracapacitors. Because of these properties, ultracapacitors are being used in many applications involving energy regeneration [4], [8]–[12].

## II. STATE OF THE ART

The research literature is replete with papers discussing energy regeneration and the use of ultracapacitors in systems, such as road vehicles [1], [7], [9], [10], industrial electric motor drive systems [11], [13], [14], vibration control and shock absorber

systems [8], [12], [15], [16], and aerospace applications [4]. However, research regarding use of these technologies in robotic systems is scarce. Here we offer a brief review and refer readers to the recent survey [17] for a more comprehensive study of the literature.

Izumi *et al.* [18] considered a dc servo system capable of regenerating excess energy into a conventional capacitor. They formulated and solved a point-to-point trajectory optimization problem for this servo system by minimizing the dissipated energy. Experimental results showed storage of excess energy in the capacitor while the motor was decelerating. In a later work Izumi [19] considered a two-link vertically articulated manipulator with energy regeneration. A point-to-point optimal trajectory problem minimizing dissipated energy was solved for this robot. Simulation results showed that the optimal trajectory reduces energy consumption compared to the conventional nonoptimized trajectory. While conventional capacitors were used, the authors pointed out the need for larger capacitances.

Fujimoto [20] found energy-minimizing trajectories for bipedal running. The problem was formulated as an optimal control problem and solved numerically for a five-link planar biped robot. The analysis took into account the possibility of energy regeneration. The optimal knee trajectory showed regions of positive and negative power. Based on the optimization results it was concluded that the use of energy regeneration mechanisms, such as, elastic actuators or back-drivable actuators combined with bidirectional power converters, can be used to reduce the overall energy consumption. Other works have focused on minimizing the cost of transport in bipedal and quadrupedal robots by optimizing joint trajectories, controls, and system parameters (e.g. link length, actuator placement, etc.) [21]–[23].

Hansen *et al.* [24] considered finding trajectories for a KUKA robot that minimize the amount of external electrical energy supplied to the motor drivers. The drivers were coupled through a common dc bus, allowing power to flow from one joint of the robot to another. However, their work did not include a capacitor to store excess energy. Thus, energy regenerated by the robot joints is wasted unless at the same time other joints utilize the regenerated energy. The authors pointed out the use of a storage capacitor as future work. Joint trajectories were described by B-splines and optimized using a gradient-based optimization method. Experimental results showed a 10% decrease in total energy consumption for the robot.

In the robotic lower-limb prostheses field, a group from the Massachusetts Institute of Technology pioneered a regenerative transfemoral prosthesis in the 1980s, which used conventional capacitors to store regenerated energy [25]–[27]. They aimed to design the system, so that no external power would be required for operation. The power required for the prosthesis was regenerated during the passive portions of gait. Results indicated the need for larger capacitances, which were not available at the time. More recent work has investigated the use of elastic elements to store the regenerated energy [3], [28]–[31]. Tucker and Fite [32] developed an analytical model of a regenerative powered transfemoral prosthesis. Energy is regenerated by controlling the actuator damping during its passive regions of operation. A regeneration manifold was found that places limits on actuator damping to achieve regeneration.

Richter [5] proposed a unifying framework for modeling and control of robots with regenerative drive systems. It enables a systematic treatment of robot motion control with explicit consideration of energy regeneration. It is capable of capturing regenerative actuators in various domains (e.g., electromechanical, hydraulic, etc.). Based on this framework, several papers have focused on the use of evolutionary algorithms and other numerical methods to find optimal system parameters that optimize a combination of motion tracking and energy enhancing objectives [33]–[40]. In addition, the authors have investigated analytical solutions to the general parameter optimization for robotic systems [41], [42]. Global closed-form solutions were found for the robot parameters (e.g., link lengths) and drive mechanism parameters (e.g., gear ratios), which maximize energy regeneration given a predefined fixed trajectory for the robot. While most efforts have focused on theory and simulations, experimental evaluations of the effectiveness of energy regeneration are very scarce in the robotics literature. Recently, the authors have developed an energy regenerative powered transfemoral prosthesis that in addition to providing natural gait for the amputee, explicitly considers energy regeneration in both hardware and control design [2]. We have developed a novel impedance controller that uses force feedback from the prosthesis shank and can operate for a wide range of walking velocities without the need for retuning. Ultracapacitors are used to store regenerated energy and also to provide energy to the prosthesis. The prosthesis prototype was tested with an amputee subject walking with different speeds on a treadmill. The results showed that under the test conditions, the amputee could walk with the prosthesis without the need for recharging.

In this paper, a generic robotic model with ultracapacitor-based regenerative drive systems is developed using the framework of Richter [5]. The problem of finding optimal point-to-point trajectories that maximize regenerative energy storage is formulated as an optimal control problem and demonstrated with a PUMA 500 robot. The direct collocation method [43] is used to find the optimal trajectories. The solutions are then implemented on a PUMA 500 robot using a semiactive virtual control (SVC) strategy [5], [44] and a standard robust passivity based controller [45]. An experimental setup is prepared to evaluate the effectiveness of energy regeneration by measuring power flows at key locations.

Section III discusses modeling of the robotic system and the regenerative drive mechanism, Section IV formulates the point-to-point trajectory optimal control problem, Section V explains the experimental procedure for evaluating the optimized trajectories, Section VI discusses the numerical and experimental optimization results for the PUMA 500 robot, and Section VII concludes this paper.

### III. MODELING

We consider general serial robots modeled with the following dynamic equations:

$$D^\circ(q)\ddot{q} + C(q, \dot{q})\dot{q} + \mathcal{R}^\circ(q, \dot{q}) + g(q) + \mathcal{T} = \tau \quad (1)$$

where  $q$  is the  $n \times 1$  vector of joint coordinates,  $D^\circ(q)$  is the inertia matrix,  $C(q, \dot{q})$  is a matrix accounting for Coriolis and

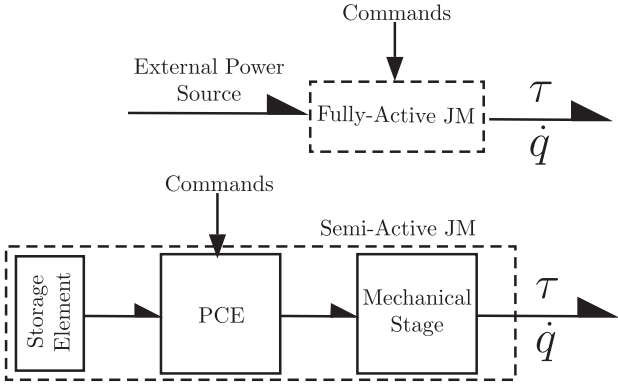


Fig. 1. Schematic of fully active and semiactive joint mechanisms. Fully active joint mechanisms use external power for actuation while semiactive joint mechanisms use an energy storing element and only exchange mechanical power with the robot.

centrifugal effects,  $\mathcal{R}^\circ(q, \dot{q})$  is a general nonlinear damping term,  $\tau$  is the vector of external forces and moments reflected to the manipulator joints,  $g(q)$  is the gravity vector and  $\tau$  is the vector of joint forces and moments applied by a set of actuators.

In this context, actuators are either conventional (termed *fully active*) or regenerative (termed *semiactive*). A fully active actuator is conventional in the sense that it exchanges mechanical power with the robot and draws electric power from an external source (similar to typical electric drives). On the other hand, semiactive actuators have self-contained energy storage. They are passive systems and only exchange mechanical power with the robot [5]. Fig. 1 depicts the concepts of fully active and semiactive actuators. Semiactive actuators are composed of a storage device to provide energy to the robot and possibly store excess energy, a power conversion element (PCE) to regulate power and to convert power between different domains, and a mechanical stage to interface with the robot.

In a general setting, a subset of manipulator joints are assumed to be semiactive, whereas the remaining joints are fully active. Also, for simplicity, the terms *actuators* and *joints* are used interchangeably.

Depending on the arrangement of the storage elements for semiactive joints, different configurations are possible [41]. We consider here the *star configuration* that consists of a single storage element connected in parallel to all the semiactive joints, Fig. 2. The star configuration provides a way to transfer power from one joint to another joint requiring energy using the common storage element as an energy reservoir. Other configurations for semiactive joints are possible, for instance a distributed arrangement where each semiactive joint uses a storage unit [41].

#### A. Semiactive Actuator Model

Bond graphs [46] are used to facilitate the representation and equation derivation. We consider electro-mechanical semiactive actuators with an ultracapacitor as the storing element and a dc motor/generator as the PCE. The same bond graph model, however, captures a wide variety of actuators in different domains.

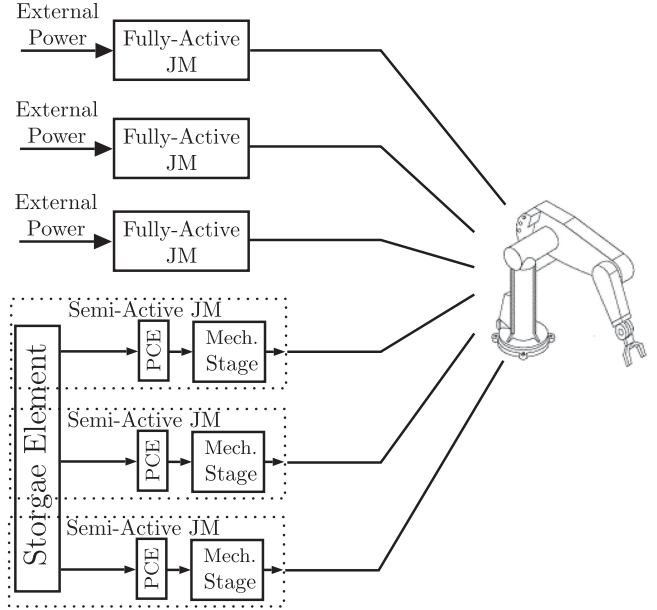


Fig. 2. Star configuration for semiactive joints. All the semiactive joints are connected to a common storage element. This allows for energy transfer from one semiactive joint to another.

Fig. 3 shows the bond graph model of the semiactive joint in the star configuration.

Each link of the robot with a semiactive joint is connected to a transmission where  $n_j$  is the velocity ratio,  $m_j$  is the inertia, and  $b_j$  is the viscous damping coefficient. The output of the transmission is connected to a dc motor/generator with torque constant  $\alpha_j$  (which equals the back-emf constant) and resistance  $R_j$ . The inertial and frictional effects of the motor/generator are assumed to have been reflected to the link side, and already included in  $m_j$  and  $b_j$ . Note that  $b_j$  is not necessarily constant and in general, it can be any nonlinear function. Power transferred to the electrical side of the motor/generator is distributed as resistive losses and as stored energy in the ultracapacitor  $C$ . An ideal four-quadrant motor driver is used to control the amount and direction of voltage applied to the dc motor where  $r_j$  is the converter voltage ratio (motor voltage over capacitor voltage). Since the motor driver does not boost the capacitor voltage,  $r_j$  is assumed to be constrained to  $[-1, 1]$ . A value  $r_j < 0$  is used to apply reverse voltage to the dc motor terminals even though the capacitor voltage is always positive. Ultracapacitors typically have very low internal resistances (in the order of  $m\Omega$ ), therefore, we have omitted the effects of internal resistance in the system model.

#### B. Augmented Model

The following interfacing torque or force  $\tau_j$  for the  $j$ th semiactive joint is derived from the bond graph model, as shown in Fig. 3:

$$\tau_j = -m_j n_j^2 \ddot{q}_j - \left( b_j n_j^2 + \frac{\alpha_j^2}{R_j} \right) \dot{q}_j + \frac{\alpha_j r_j}{R_j} V_{cap} \quad (2)$$

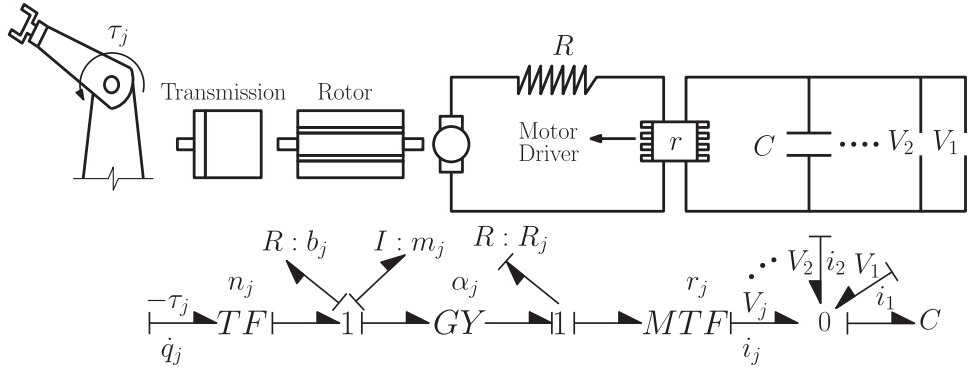


Fig. 3. Bond graph of electro-mechanical semiactive joint mechanism in the star configuration.

where  $V_{\text{cap}}$  is the capacitor voltage, and  $a_j = \alpha_j n_j$ . Replacing  $\tau_j$  from (2) into (1) and absorbing the terms containing  $\dot{q}$  and  $\ddot{q}$  into the right-hand side, the augmented model is obtained as

$$D(q)\ddot{q} + C(q,\dot{q})\dot{q} + \mathcal{R}(q,\dot{q}) + g + \mathcal{T} = u \quad (3)$$

where  $D$  and  $\mathcal{R}$  are

$$\begin{aligned} D_{ij} &= D_{ij}^{\circ} & i \neq j \\ D_{jj} &= D_{jj}^a & j \notin \mathcal{I}_{\text{sa}} \\ D_{jj} &= D_{jj}^{\circ} + m_j n_j^2 & j \in \mathcal{I}_{\text{sa}} \\ \mathcal{R}_j &= \mathcal{R}_j^a & j \notin \mathcal{I}_{\text{sa}} \\ \mathcal{R}_j &= \mathcal{R}_j^{\circ} + \left( b_j n_j^2 + \frac{a_j^2}{R_j} \right) & j \in \mathcal{I}_{\text{sa}} \end{aligned} \quad (4)$$

and

$$u = \begin{cases} v_j & j \notin \mathcal{I}_{\text{sa}} \\ \frac{a_j r_j}{R_j} V_{\text{cap}} & j \in \mathcal{I}_{\text{sa}} \end{cases} \quad (5)$$

where  $\mathcal{I}_{\text{sa}}$  is the index set of the semiactive joints and the  $a$  superscript indicates that the matrices already include inertial and damping properties for the active joints. Fully active joints are directly controlled with  $v_j$ , which is typically an analog input voltage to a torque-mode servo amplifier. For the semiactive joints, only the voltage ratio  $r_j$  is available as a control variable. Control is achieved with the semiactive virtual control method summarized next.

### C. Semiactive Virtual Control Strategy

To control a robot with fully active and semiactive joints, a *virtual control law* ( $\tau^d$ ) is first designed for  $u$  in the augmented model (3). For fully active joints, this law is enforced directly, using externally-powered servo drives. For semiactive joints, the control input  $r_j$  is adjusted such that the following *virtual matching* relation holds

$$\frac{a_j r_j}{R_j} V_{\text{cap}} = \tau_j^d. \quad (6)$$

The virtual control ( $\tau^d$ ) can be any feedback law compatible with the desired motion control objectives for the augmented model.

If virtual matching (6) holds exactly at all times, any properties that apply to the virtual design such as, stability, tracking performance, and robustness will be propagated to the actual system [5]. The modulation law for exact virtual matching is simply obtained by solving for  $r_j$  from (6). Virtual matching is always possible as long as there is a positive voltage in the capacitor, and it will hold exactly whenever  $a_j/R_j$  is precisely known and the calculated  $r_j$  is within  $[-1, 1]$ . Also, note that the virtual control law (6) and the augmented model (3) were derived *without the need to model the ultracapacitor*. Ultracapacitor models are in general complex and nonlinear and do not cover all the aspects of the ultracapacitor's performance [47]–[50]. Placing the capacitor voltage in feedback of the virtual control law allows dynamics and control analysis without the modeling complexities associated with ultracapacitors. Furthermore, as with any system with finite on-board power storage, operation must be stopped once charge (indicated by  $V_{\text{cap}}$ ) drops below an acceptable threshold and the system gets recharged. It is important to note that self-sustained operation or even charge buildup can occur, depending on system parameters and trajectories [5], [41], [42], [44].

### D. Regenerated Energy

The energy provided to or extracted from the capacitor by the  $j$ th semiactive joint ( $\Delta E_j$ ) can be derived from the bond graph representation of Fig. 3 as

$$\Delta E_j = \int_{t_1}^{t_2} v_j i_j dt \quad (7)$$

where in the star configuration,  $v_j$  is equal to the capacitor voltage  $V_{\text{cap}}$ , and

$$i_j = \frac{r_j}{R_j} (a_j \dot{q}_j - r_j v_j). \quad (8)$$

Replacing for  $i_j$  and  $v_j$  in (7),

$$\Delta E_j = \int_{t_1}^{t_2} \frac{r_j}{R_j} (a_j V_{\text{cap}} \dot{q}_j - r_j V_{\text{cap}}^2) dt. \quad (9)$$

Using (6), the following  $\Delta E_j$  can be written in terms of  $\tau^d$ :

$$\Delta E_j = \int_{t_1}^{t_2} \left( \tau_j^d \dot{q}_j - \frac{R_j}{a_j^2} (\tau_j^d)^2 \right) dt. \quad (10)$$

By summing up the energies provided to the capacitor by all the semiactive joints, the total energy is found to be

$$\Delta E = \int_{t_1}^{t_2} \sum_{j=1}^e \left( \tau_j^d \dot{q}_j - \frac{R_j}{a_j^2} (\tau_j^d)^2 \right) dt. \quad (11)$$

A value of  $\Delta E > 0$  indicates energy regeneration and  $\Delta E < 0$  indicates energy consumption in the specified time interval. Note again that as a result of SVC, the above derivation is independent of the ultracapacitor model and is only a function of the control law  $\tau^d$ , joint velocities  $\dot{q}$ , and joint parameters  $R$  and  $a$ . In other words, SVC decouples the dynamics of the robot and energy regeneration from the dynamics of the ultracapacitor.

An external energy balance for the whole robotic system can be derived as

$$W_{\text{act}} = W_{\text{ext}} + \Delta E_m^T + \Sigma_m^T + \Delta E_s + \Sigma_e \quad (12)$$

where  $W_{\text{act}}$  is the work done by the fully active joints,  $W_{\text{ext}}$  is the work done by the external forces and moments,  $\Delta E_m^T$  and  $\Sigma_m^T$  are the total mechanical energy and mechanical losses of the robot and the semiactive joints, respectively,  $\Delta E_s$  is the energy stored in the capacitor and  $\Sigma_e$  are the Joule losses of the semiactive joints. This equation shows that the energy stored in the capacitor is the net result of  $W_{\text{act}}$ ,  $W_{\text{ext}}$ , and  $\Delta E_m^T$  minus all losses. The details of the derivation of (12) may be found in [51]. In Section IV, we formulate a trajectory optimization problem based on maximizing (11).

#### IV. FORMULATING THE OPTIMIZATION PROBLEM

We aim to find trajectories that maximize the amount of energy regenerated when the robot starts from an initial configuration at time zero, and moves to a final configuration at some specified time. For this purpose, the problem is formulated as an optimal control problem of finding the vector of optimal trajectories  $(q(t), \dot{q}(t), \ddot{q}(t))$  and the vector of optimal controls  $(\tau^d)$  that maximize (11)

$$\max_{\tau^d, q} J = \int_{t_1}^{t_2} \sum_{j=1}^e \left( \tau_j^d \dot{q}_j - \frac{R_j \tau_j^d}{a_j^2} \right) dt \quad (13)$$

while being subjected to the dynamic equations of the robot (3), bounds on the control, and constraints for the starting and ending points of the trajectories

$$D(q)\ddot{q} + C(q, \dot{q})\dot{q} + \mathcal{R}(q, \dot{q}) + g(q) + \mathcal{T} = \tau^d \quad (14a)$$

$$\frac{-a_j}{R_j} V_{\text{cap}} \leq \tau_j^d \leq \frac{a_j}{R_j} V_{\text{cap}} \quad (14b)$$

$$q_{t=0} = q_i \quad \dot{q}_{t=0} = \dot{q}_i \quad (14c)$$

$$q_{t=t_f} = q_f \quad \dot{q}_{t=t_f} = \dot{q}_f \quad (14d)$$

The bounds for the controls  $\tau^d$  are obtained from the requirement  $|r_j| \leq 1$  and (6), where the available capacitor voltage  $V_{\text{cap}}$  is assumed constant for the purposes of the optimization. Trajectories start from the initial position  $q_i$  and initial velocity  $\dot{q}_i$ , and reach the final position  $q_f$  with final velocity  $\dot{q}_f$  at time  $t_f$ .

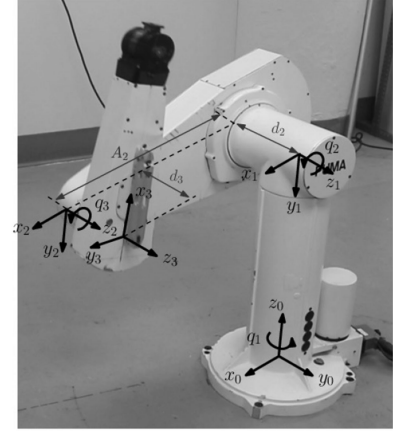


Fig. 4. PUMA 500 robot used as a case study for finding optimal trajectories that maximize energy regeneration. Coordinate frames are assigned using the Denavit–Hartenberg convention.

TABLE I  
STARTING AND ENDING CONSTRAINTS (IN JOINT SPACE) FOR THE THREE OPTIMAL TRAJECTORIES

	$q_i(\text{rad})$	$q_f(\text{rad})$	$t_f(s)$
Case 1	$[0, -2\pi/5, 0]$	$[\pi/3, 0, \pi/4]$	2
Case 2	$[0, \pi/4, -\pi/4]$	$[-\pi/4, -3\pi/4, 0]$	4
Case 3	$[0, -\pi/4, \pi/4]$	$[\pi/2, -\pi/4, \pi/4]$	8

Trajectories start at point A ( $q_i, \dot{q}_i$ ) and terminate at time  $t_f$  at point B ( $q_f, \dot{q}_f$ ). Initial and terminal joint velocities are zero for the three trajectories (i.e.  $\dot{q}_i = [0, 0, 0]$  and  $\dot{q}_f = [0, 0, 0]$ ).

As a case study, we consider finding optimal trajectories for a PUMA 500 robot. However, the methods used here are applicable to any robotic manipulator that can be modeled as in (3). The PUMA robot shown in Fig. 4, consists of three main joints and spherical wrist, which together provide six degrees of freedom for the robot. Here, we only consider the dynamics of the three main joints of the robot that have the most potential for energy regeneration. The three main joints,  $q_1$ ,  $q_2$ , and  $q_3$ , are assumed to be semiactive and connected in the star configuration via a central ultracapacitor. The robot is constrained to start from the initial position  $q_i$  (in joint space) and initial velocity  $\dot{q}_i = [0, 0, 0]$  – referred to as Point A – and finish at  $q_f$  with  $\dot{q}_f = [0, 0, 0]$  – referred to as Point B. Three optimal trajectories with different starting and ending positions are considered. These points are given in Table I and also shown in Fig. 5.

Using the linear parameterization property for robotic manipulators [45], and assuming no external forces and moments are applied to the robot ( $\mathcal{T} = 0$ ), the dynamic equations (14a) can be written as

$$Y(q, \dot{q}, \ddot{q})\theta + \mathcal{R}(q, \dot{q}) = \tau^d \quad (15)$$

where  $Y_{n \times p}$  is the regressor matrix,  $\theta_{p \times 1}$  is the parameter vector that is a function of the physical parameters of the system (e.g. link lengths, link masses, gear ratios etc.) and  $\mathcal{R}$  includes the nonlinear damping and frictional effects for the robot joints



Fig. 5. Initial (Point A) and final (Point B) configurations for the three studied cases. First row: case 1. Second row: case 2. Third row: case 3. First column: initial configuration. Second column: final configuration.

and the drive mechanism. Using the Denavit–Hartenberg (DH) convention [45], dynamic equations for the PUMA robot and the semiactive drive mechanisms are derived. These equations are presented in regressor and parameter vector form in Appendix A, alongside system parameters and methods that were used to identify them. Fig. 4 shows coordinate frames assigned for the PUMA robot using the DH convention.

The optimal control problem defined in (13) and (14) is in general nonlinear and nonconvex. It can have none, one, many, or an infinite number of solutions. When no immediate analytical solution exists, one normally resorts to numerical methods for solving the problem. The optimality conditions for this problem generally lead to a set of differential equations with split boundary conditions. Methods such as, steepest descent and variation of extremals may be used for solving these type of two-point boundary value problems [52].

After deriving dynamic equations for the PUMA robot and the regenerative semiactive joints, we use the method of direct collocation [36], [43], [53] to transcribe the optimal control problem into a large-scale nonlinear program problem. In this method, the states ( $q, \dot{q}$ ) and controls ( $\tau^d$ ) are discretized into  $N$  temporal

nodes. The cost function (13) and constraints (14) are discretized by using an appropriate finite difference approximation for the state derivatives. We use the backward Euler approximation in this paper. The cost function becomes a function of the states and controls at each grid point, and the dynamic constraints are converted into a set of algebraic constraints that are also a function of the discretized states and controls. The optimal control problem is converted to a constrained optimization problem of finding the states and controls at each grid point that minimize the discretized cost function and satisfy a set of algebraic constraints.

By observing the overall energy balance equation (12) for our case study, since all the robot joints are semiactive ( $W_{\text{act}} = 0$ ), there are no external forces or moments being applied to the system ( $W_{\text{ext}} = 0$ ), and the initial and final configurations of the robot are constrained ( $\Delta E_m^T$  is constant), maximizing  $\Delta E_s$  is equivalent to minimizing energy consumption ( $W_{\text{ext}} - \Delta E_s$ ), and equivalent to minimizing electrical and mechanical losses ( $\Sigma_m^T + \Sigma_e$ ). Note that both positive and negative portions of power are integrated to form  $\Delta E_s$  in these equivalent optimizations. The nonregenerative case, however, includes only the positive portions of the power profile, and maximizing  $\Delta E_s$  is equivalent to minimizing consumption from an external source and yields different solutions.

## V. EXPERIMENTAL SETUP

Fig. 6 shows the schematic of the experimental setup. The PUMA 500 robot has three main joints and three joints at the wrist. Here we are only concerned with the operation of the main three joints that have the most potential for energy regeneration. Each joint is actuated by a dc motor that is driven by the four quadrant 25 amp SyRen motor driver (Dimension Engineering, Hudson, Ohio). The dSPACE 1103 controller board (dSPACE GmbH, Paderborn, Germany) is used for controlling the robot and for data acquisition. The input and output voltages and currents for each motor driver are needed to calculate the instantaneous power. The currents are measured via the ACS723 current sensors (Allegro Microsystems, Worcester, Massachusetts). The capacitor voltage is directly measured with a voltage divider and the dSPACE system. The voltage on the motor side is not directly measured, however, it is verified separately that this voltage accurately follows the voltage requested by the command signal ( $V_{\text{Command}}$ ). The input of all three motor drivers are connected to a common 48 V ultracapacitor bank (Maxwell Technologies, San Diego, California) with a capacitance of 165 F. The capacitor is initially charged to 27 V to avoid reaching the 30 V absolute maximum input voltage for the motor drivers. A robust passivity based control method is used to track the optimal trajectories found in Section VI. The controller is implemented in real time using angular position and velocity feedback from encoders, in addition to capacitor voltage feedback.

### A. Overview of Robust Passivity Based Control

The optimization problem yields an open-loop control solution that is not implementable in the real robot. The robust passivity based control [45] was selected to ensure the robot

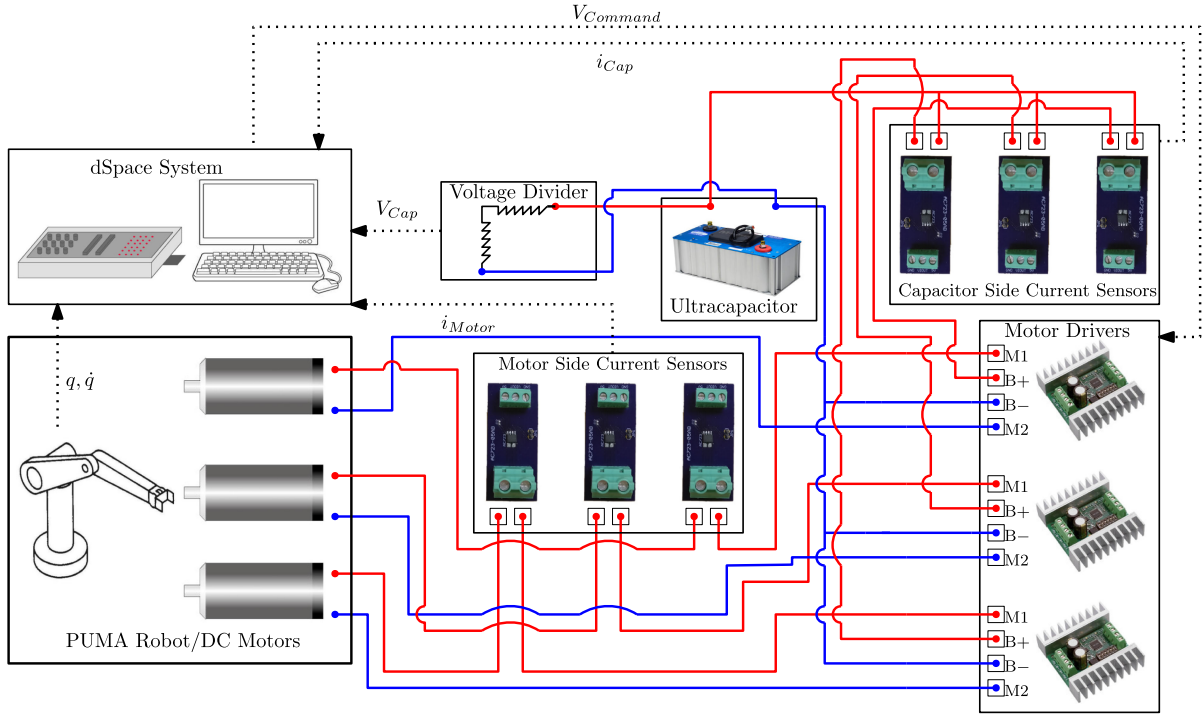


Fig. 6. Schematic of the experimental setup. Current sensors are used to measure currents on both sides of each motor driver. Voltage on the capacitor side is measured directly via the dSPACE system, also used for controlling the robot. The motor drivers are all connected to a common ultracapacitor. Dotted lines indicate signals, solid lines indicate wiring.

tracks the desired optimal trajectories with guaranteed stability against parametric uncertainties in the robot model. Based on the dynamic equation for the augmented model (3) and assuming no known external forces or moments are exerted on the robot ( $\mathcal{T} = 0$ ), the control input is chosen as

$$\tau^d = \hat{D}a + \hat{C}\nu + \hat{\mathcal{R}} + \hat{g} - Kr = Y_a(q, \dot{q}, a, v)\hat{\theta} - Kr \quad (16)$$

where  $Y_a$  is the control regressor and  $\hat{\theta}$  is the parameter estimate adjusted by the control law. Variables  $a$ ,  $v$ , and  $r$  are defined as

$$v = \dot{q}^d - \Lambda\tilde{q} \quad (17a)$$

$$a = \dot{v} \quad (17b)$$

$$r = \dot{q}^d - \nu \quad (17c)$$

where  $q^d$  and  $\dot{q}^d$  denote the desired joint trajectories and  $\tilde{q} = q - q^d$  denotes the tracking error. Also,  $K$  and  $\Lambda$  are diagonal matrices with positive nonzero entries. The parameter estimate  $\hat{\theta}$  is adjusted according to

$$\hat{\theta} = \theta_0 + \delta\theta \quad (18)$$

where  $\theta_0$  is a set of constant nominal parameters. If the parametric uncertainty satisfies  $\|\theta - \hat{\theta}\| \leq \rho$ , then choosing  $\delta\theta$  as

$$\delta\theta = \begin{cases} -\rho \frac{Y_a^T r}{\|Y_a^T r\|} & \text{if } \|Y_a^T r\| > \epsilon \\ -\frac{\rho}{\epsilon} Y_a^T r & \text{if } \|Y_a^T r\| \leq \epsilon \end{cases} \quad (19)$$

where  $\epsilon$  is a small positive parameter, yields ultimate boundedness of the tracking error.

## VI. RESULTS: NUMERICAL OPTIMIZATION AND EXPERIMENTS

The code used to solve the problem considered in this paper is available in the supplementary material and also can be downloaded from [54]. The direct collocation problem is solved using the interior point optimizer numerical solver [55]. The IPOPT solver generally finds local optima for nonlinear problems. The optimization was run several times starting from different random initial conditions to find the best possible solution. Successive mesh refinement was used until the solution was insensitive to the actual of  $N$ , which was achieved with  $N = 100$ . Each optimization problem was solved in 400 to 900 iterations, depending on the case and the initial conditions, and took 25 to 55 s on a computer equipped with *Intel Core i7-5600U CPU* running *Matlab R2018a*.

For each case, the optimization was run once from a starting point A to the final point B, and once from B back to A. The capacitor voltage during the optimization was assumed to be a constant 27 V. This corresponds to control torques in  $[-149, 149]$  Nm,  $[-224, 224]$  Nm and  $[-152, 152]$  Nm for Joints 1, 2, and 3, respectively.

Fig. 7 shows optimal and actual trajectories followed by the robot joints for each case. Videos of the motion trajectories are also included in the supplementary material and can also be found in [56]. The robust passivity based controller provides good tracking, however, a small error (0.046 rad) is observed. In Fig. 7, the control torque saturates at  $-222$  Nm for Joint 2 in cases 1 and 2. This value is higher than the limit used in the optimization, which was based on a constant capacitor voltage of 27 V. However, the capacitor voltage is variable. In Case 1,

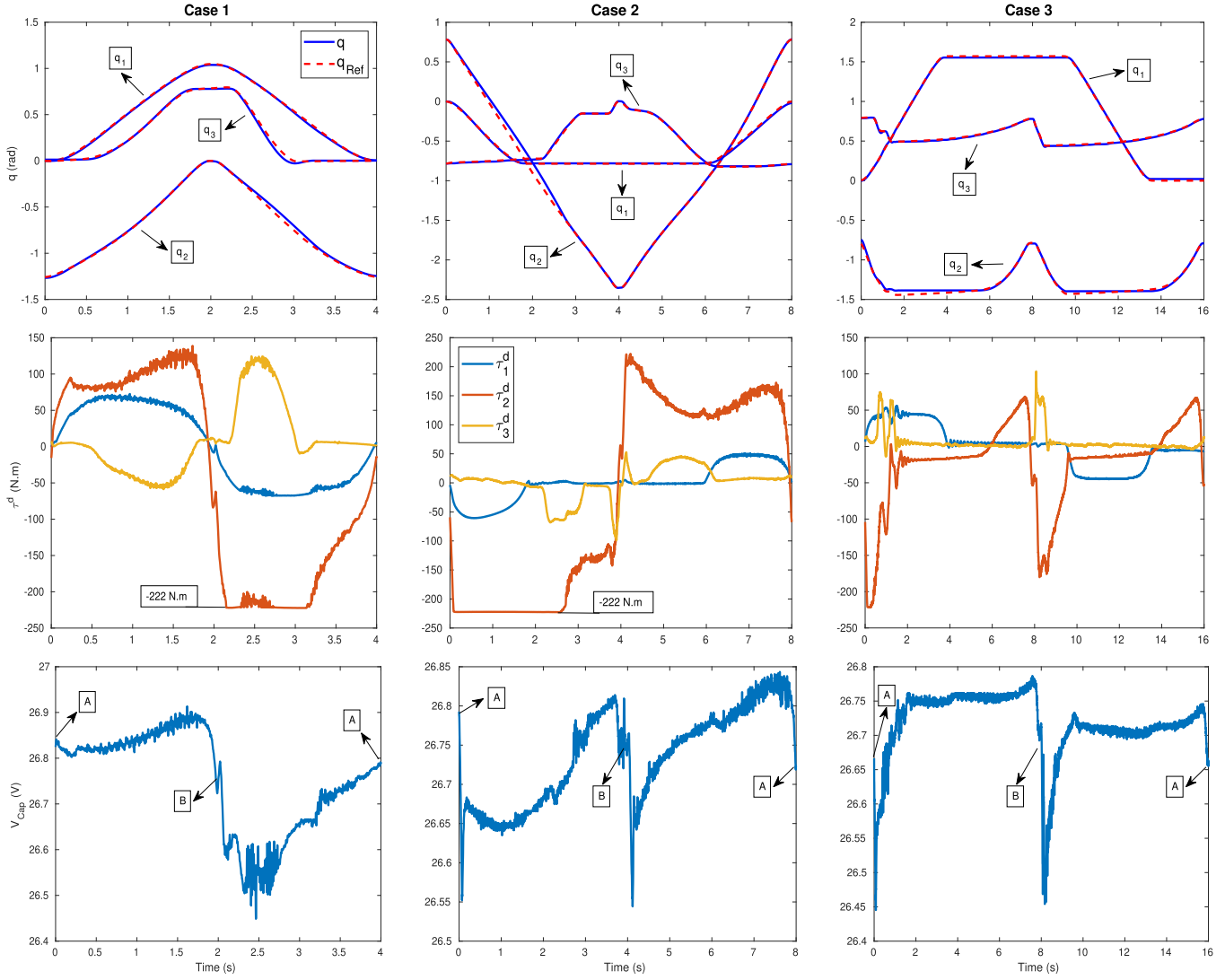


Fig. 7. First row: optimal reference trajectories (dotted lines) and actual trajectories (solid lines) followed by the PUMA 500 robot. Trajectories go from point A to point B, and vice versa. Second row: control torque commands ( $\tau^d$ ) applied to the robot joints. Third row: capacitor voltage during the movement of the robot.

the capacitor has 26.84 V at the beginning of the movement and varies between 26.91 and 26.45 V. Since this is smaller than 27 V, saturation of  $r$  and loss of tracking occur. One could achieve more accurate results by including the ultracapacitor model in the optimization, however, doing so would significantly increase the complexity of the problem. Ultracapacitors exhibit nonlinear and complex behavior and their models, and do not represent all the aspects of the ultracapacitor's performance [47]–[50]. By feeding back the capacitor voltage, SVC allows the control of the robot without being concerned with the nonlinear behavior of the ultracapacitor. In addition, for the robot joints that do not reach the torque saturation limit, better tracking performance could have been achieved by increasing the gains of the robust controller, however, as explained later, higher gains lead to control signal chattering, which in turn results in significant reduction of motor driver efficiency to regenerate energy.

Fig. 8 shows power flows for the motor and capacitor sides of the motor drivers. Power is positive when it flows from the ultracapacitor to the motor driver and to the robot joints. Table II

summarizes the energy consumed by the robot while following the optimal trajectories, where negative consumption indicates energy regeneration. Fig. 8 also compares the measured power with the power predicted by the robot model when following optimal trajectories. In general, the predicted power agrees quite well with the power on the motor side, indicating that a very good model was identified for the system. Results also show that the power on the capacitor side is higher than the power on the motor side. This reflects the inefficiency of the motor driver (some power is dissipated in the motor driver) and also the power required to operate them. These inefficiencies are not taken into account by the optimization, which considers an ideal motor driver.

Observing the external energy equation (12), we note that all joints are semiactive ( $W_{act} = 0$ ) and no external forces or moments are present ( $W_{ext} = 0$ ), therefore, energy stored in the ultracapacitor can only be a result of a change in the mechanical energy of the system. In Case 1, the robot trajectory starts from a higher potential energy level compared to the ending

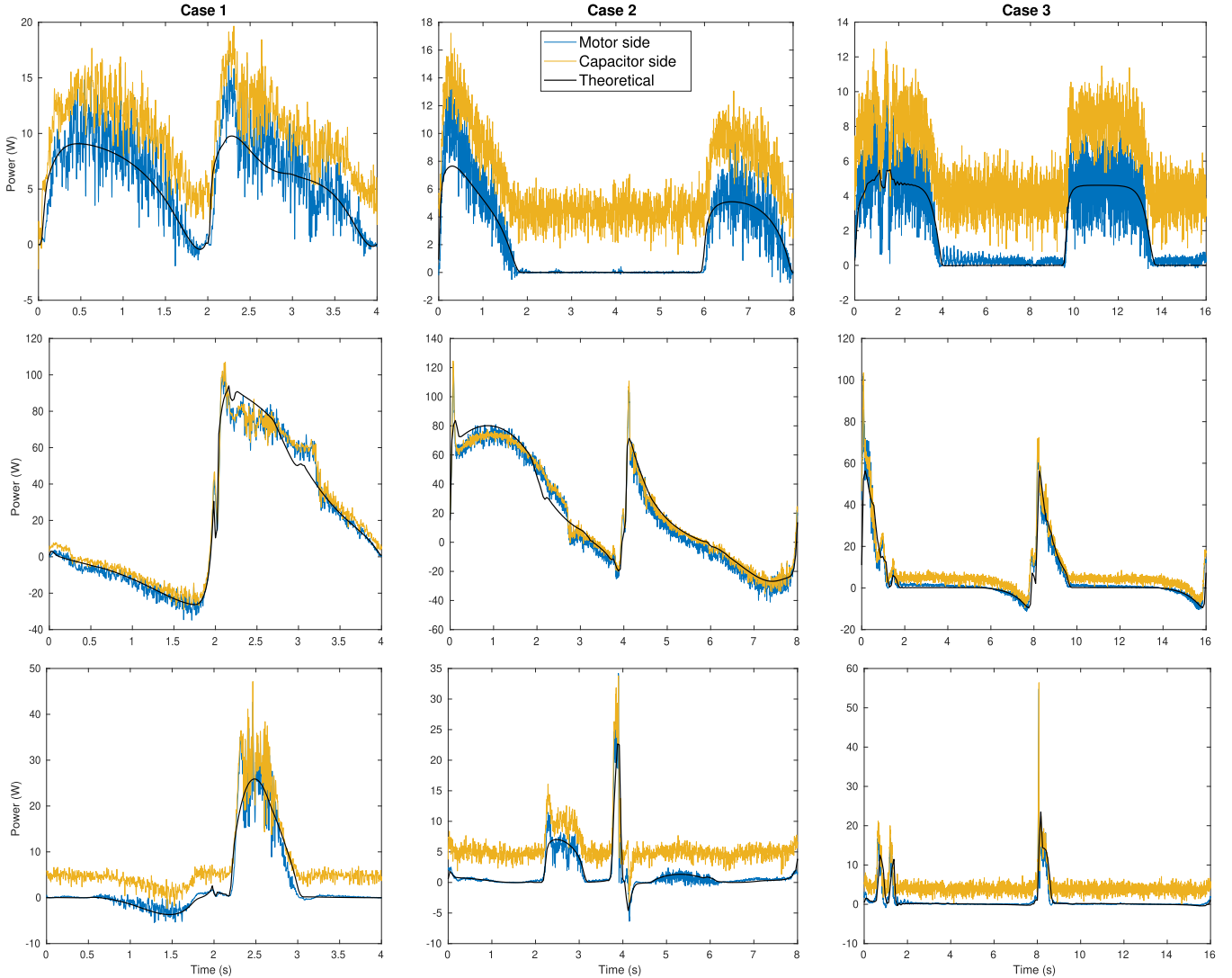


Fig. 8. Power flows for the motor side and capacitor side of the motor driver for (a) Joint 1, (b) Joint 2, and (c) Joint 3. Positive power indicates energy consumption and negative power indicates energy regeneration. The theoretical power flow is also shown for comparison.

configuration while going from *A* to *B*. As a result, a portion of this difference is regenerated and stored in the ultracapacitor by Joints 2 and 3, and the rest is lost as electrical and mechanical losses. Joint 2 is the main contributor to energy regeneration ( $-24.14$  J from *A* to *B* with peak negative power of  $-35$  W) due to motion in a vertical plane and a large weight, whereas Joint 1 mostly consumes energy ( $12.10$  J) and only regenerates at the end of the *A* to *B* portion when the joint is braking and reversing direction. Joint 3 shows portions of negative power on the motor side ( $-1.5$  J energy is regenerated from *A* to *B* on the motor side), however, power on the capacitor side is only positive ( $7.5$  J is consumed on the capacitor side), indicating that the regenerated energy is all dissipated in the motor driver and does not reach the capacitor. In the *B* to *A* portion, power is positive and energy flows from the capacitor to the robot ( $12.34$ ,  $99.42$ , and  $14.55$  J for Joints 1, 2, and 3, respectively). Part of this power is stored as potential energy to move the robot back to point *A* and the rest is lost due to mechanical and electrical losses.

In the *A* to *B* portion of Case 2, the robot starts at a low elevation, goes through an almost vertical position ( $q_2 \approx -\pi/2$  and  $q_3 \approx 0$ ), and comes down to its final configuration. For Joint 2, this result in energy being consumed and converted to potential energy when the robot is moving to a higher potential energy level (from  $q_2 = \pi/4$  to  $q_2 \approx -\pi/2$ ), and regenerated when the robot is moving to a lower potential energy level (from  $q_2 \approx -\pi/2$  to  $q_2 = -3\pi/4$ ). Similarly in the *B* to *A* portion, power is positive while moving to a higher potential energy level ( $q_2 = -\pi/4$  to  $q_2 \approx -\pi/2$ ), and regenerated when going to lower potential energy levels ( $q_2 \approx -\pi/2$  to  $q_2 = \pi/4$ ). Joint 2 is the main contributor to energy regeneration (negative power peak  $-41$  watts). From *A* to *B* Joint 2 consumes a net energy of  $160.37$  J, and from *B* to *A* it regenerates a net of  $-8.62$  J. Joint 3 is mostly consuming energy and only regenerates when the joint is braking and reversing at the end of the *A* to *B* portion, and Joint 1 is consuming energy throughout the movement of the robot.

TABLE II  
ENERGY CONSUMPTION FOR THE PUMA 500 ROBOT WHEN FOLLOWING  
OPTIMAL TRAJECTORIES

Case 1							
	$E_{A \rightarrow B}(J)$		$E_{B \rightarrow A}(J)$				
	Motor	Capacitor	Motor	Capacitor			
Joint 1	12.10	20.16	12.34	20.07			
Joint 2	-24.14	-16.21	99.42	103.76			
Joint 3	-1.50	7.53	14.55	22.80			
Total	-13.54	11.48	126.31	146.63			
Case 2							
	$E_{A \rightarrow B}(J)$		$E_{B \rightarrow A}(J)$				
	Motor	Capacitor	Motor	Capacitor			
Joint 1	10.34	27.11	7.92	25.72			
Joint 2	160.37	168.84	-8.62	7.07			
Joint 3	9.51	27.33	1.66	19.73			
Total	180.22	223.28	0.96	52.52			
Case 3							
	$E_{A \rightarrow B}(J)$		$E_{B \rightarrow A}(J)$				
	Motor	Capacitor	Motor	Capacitor			
Joint 1	18.68	46.88	17.20	46.67			
Joint 2	42.62	70.10	35.64	63.77			
Joint 3	7.05	37.08	7.84	37.47			
Total	68.35	154.06	60.68	147.91			

Energy consumption is reported for the motor side and capacitor side of the motor driver, when going from point A to point B and vice versa. Negative energy indicates energy regeneration.

The initial and final configurations in Case 3 are chosen such that the robot can reach the final configuration by only moving Joint 1. However, maintaining Joints 2 and 3 at their initial configuration is energy costly. The optimal trajectory moves the robot to a low energy consuming configuration where the power flow for Joints 2 and 3 are close to zero. The robot only moves out of the low energy configuration at the end of the trajectory to reach the final configuration. Similar to Cases 1 and 2, Joint 2 regenerates energy while moving to a lower potential energy level.

Note that in portions of the robot's movement, when Joint 2 is regenerating energy and Joints 1 and 2 are consuming energy, energy is being channeled from Joint 2 to the other robot joints through the capacitor.

In addition, note that ultracapacitors exhibit complex and nonlinear dynamic behavior due to the capacitance and equivalent series resistor being a function of voltage and frequency [47],

[57]. The SVC allows us to control the robot without being concerned with the nonlinearities and complexities of ultracapacitor behavior and their effect on the overall performance of the robot.

Fig. 10 shows Sankey diagrams for the overall energy balance for Case 1 based on (12) and using model parameters(refer to Appendix A). Since there is no energy entering the system from an external source (i.e.  $W_{\text{ext}} = 0$  and  $W_{\text{act}} = 0$ ), energy can be stored in the capacitor only due to changes in mechanical energy ( $\Delta E_m^T$ ). Also, since the robot trajectories start and end at a stationary configurations (i.e.  $\dot{q}_s = \dot{q}_f = [0, 0, 0]$ ), the mechanical energy difference between points A to B is equal to the potential energy difference. This potential energy difference is 56.40 J for Case 1. In the first portion of the movement, about 49% of the mechanical energy is dissipated as mechanical losses, another 27% is dissipated as electrical losses, and only about 24% reaches the motor drive. Due to inefficiencies in the motor drive only part of that energy is actually stored in the capacitor; however, by utilizing a high efficiency drive these additional losses can be minimized. In the second portion of the movement, 126.31 J of energy is provided by the driver to move the robot from point B to point A. Mechanical losses account for about 27% of the provided energy, electrical losses account for about 28% of the provided energy, and only 45% is stored as mechanical energy. These figures indicate that the mechanical losses, which are due to the design of the robot, are a large portion of the total losses and a better robot design can lead to more energy regeneration.

#### A. Consumption Minimization Without Regeneration

The problem of minimizing energy consumption in robots with nonregenerative drives or storage elements has been widely studied. It is useful to point out the differences with our approach, both methodologically and in terms of intended application scenarios. We consider robots containing on-board energy storage devices, in this case supercapacitors. Many applications exist where the robot is not connected to an external power source, for instance mobile manipulators, space robots, and prosthetic and orthotic devices. In these cases it is important to maintain and monitor the stored charge explicitly rather than merely minimize energy draw. The experimental demonstration used an industrial robot connected to a single supercapacitor, but the methodology is equally applicable to the above mentioned areas.

Nonregenerative robot drives must dissipate the return power associated with robot motion cycles, and will -by definition- yield higher energy consumption in comparison with a regenerative solution *for the same joint trajectories*. However, the question arises whether the optimization problem formulated without regeneration can generate different optimal trajectories and possibly a smaller energy consumption.

To help answer this question with the methods of this paper, we regard the single supercapacitor as an external constant-voltage power source and minimize energy draw through trajectory optimization using IPOPT. To capture the absence of regeneration, the cost function of (13) is modified by saturating each negative joint power to zero. The cost function will then represent energy consumption. The dynamics of the robot

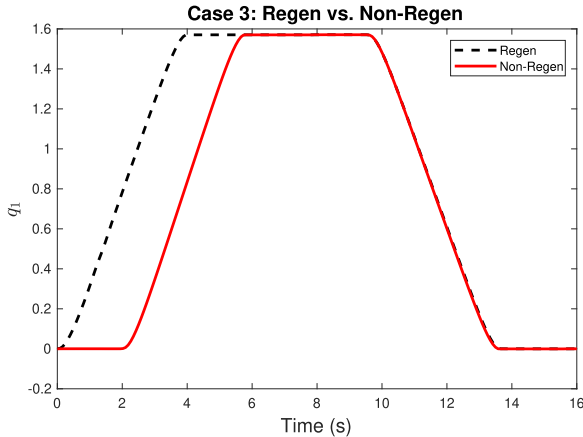


Fig. 9. Optimum and neighboring trajectories followed by the robot when going from point A to point B in Case 1. Neighboring trajectories are tested to show the effectiveness of the optimization.

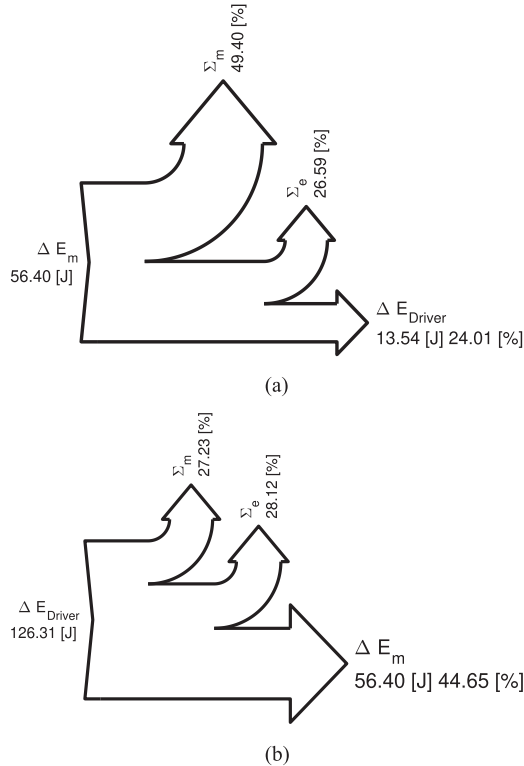


Fig. 10. Sankey diagram showing the overall energy balance for the PUMA 500 robot when following optimal trajectories in Case 1 form (a) A to B and (b) B to A. The overall mechanical energy of the robot is represented by  $\Delta E_m$ ,  $\Sigma_e$  and  $\Sigma_m$  are the electrical and mechanical losses respectively,  $\Delta E_{Driver}$  is the energy going to (i.e. regenerated) or coming from (i.e. consumed) the motor driver.

dicate that motor power must be bidirectional for cyclic acceleration and deceleration. Negative power can be regarded as having been dissipated in the nonregenerative electronics.

A significant difference in the optimal trajectories was found for Joint 1 in Case 3, as shown in Fig. 9. Table III shows a

TABLE III  
OPTIMAL ENERGY CONSUMPTION FOR THE PUMA 500 ROBOT WITH AND WITHOUT REGENERATION FOR CASE 3

Case 3				
$E_{A \rightarrow B}(J)$		$E_{B \rightarrow A}(J)$		
	Regen	Non-Regen	Regen	Non-Regen
Joint 1	16.58	16.47	16.44	16.45
Joint 2	33.21	40.47	33.32	40.51
Joint 3	6.59	6.854	6.745	6.982
Total	56.38	63.80	56.50	63.94

The optimal trajectories for Joint 1 were significantly different. The absence of negative power transients in Joint 2 results in an increased consumption compared with the regenerative case.

comparison of energy consumption for all joints. The nonregenerative optimal trajectories for Joints 1 and 3 produce practically the same consumption as in the regenerative case. However, the absence of return power in Joint 2 results in a higher overall energy consumption in the nonregenerative case.

Results for Cases 1 and 2 are omitted for conciseness, however, it was observed that the joints and motions having the lowest regeneration potential (lightweight joints and small potential energy differences between the initial and final positions) could give smaller energy consumption in the nonregenerative optimization. But the effect of disabling regeneration in cases with high potential dominated the results and gave an overall higher consumption. The results conclusively show that minimizing consumption in a nonregenerative system is not the same as maximizing storage in the regenerative case, and that separate optimizations must be conducted.

We define the effectiveness of energy regeneration as

$$\epsilon = 1 - \frac{\Delta E_R}{\Delta E_{NR}} \quad (20)$$

where  $\Delta E_R$  is the energy consumed by the robot in one complete cycle when energy regeneration is enabled,  $\Delta E_{NR}$  is the energy consumed by the robot in one complete cycle when no energy regeneration capability exists.  $\Delta E_{NR}$  is computed by integrating the power flows for each joint assuming all negative power is dissipated (i.e.  $P(P < 0) = 0$ ). The effectiveness is a number between 0 and 1, where  $\epsilon = 0$  indicates that energy regeneration has no effect in reducing the energy consumption of the robot, and  $\epsilon = 1$  indicates that energy regeneration reduces energy consumption by 100%.

This measure is first used with the optimal regenerative trajectories as a basis for comparison. For Case 1,  $\Delta E_R = 113$  J and  $\Delta E_{NR} = 141$  J, which results in  $\epsilon = 0.2$ , that is, a 20% reduction in energy consumption. We use the motor side energy to compute  $\epsilon$  to exclude the deficiencies of the motor driver. For Cases 2 and 3, the reductions in energy consumption are 22% reduction and 10%, respectively.

Using the optimal trajectories calculated for the nonregenerative case, the reduction in energy consumption calculated from

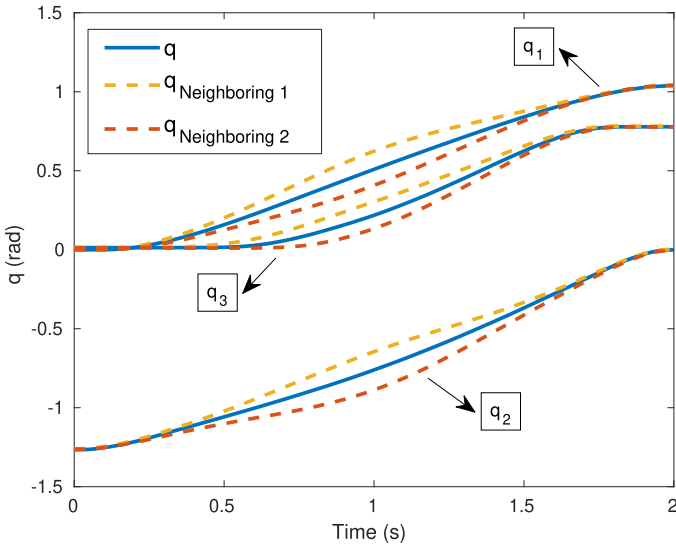


Fig. 11. Optimum and neighboring trajectories followed by the robot when going from point A to point B in Case 1. Neighboring trajectories are tested to show the effectiveness of the optimization.

TABLE IV  
COMPARISON OF ENERGY CONSUMPTION FOR THE PUMA 500 ROBOT WHEN FOLLOWING OPTIMAL AND NEIGHBORING TRAJECTORIES

	$E_{A \rightarrow B}(J)$		
	Neighboring 1	Neighboring 2	Optimal
Joint 1	12.96	12.95	<u>12.10</u>
Joint 2	-21.25	-22.05	<u>-24.14</u>
Joint 3	<u>-1.91</u>	-1.10	-1.50
Total	-10.20	-10.20	<u>-13.54</u>

Energy consumption is reported for the motor side of the motor driver, when going from point A to point B in Case 1. Negative energy indicates energy being regenerated. The neighboring trajectories show a lower amount of total energy regeneration when compared to the optimal trajectory.

Table III is 12%. For Cases 1 and 2, savings were calculated to be 19% and 17%, respectively.

### B. Neighboring Trajectories and Sensitivity

To verify that the optimum trajectories are in fact maxima and to explore the sensitivity of the optimal solution, two neighboring trajectories are generated and evaluated. In the interest of conciseness, we only consider the A to B portion of Case 1. Neighboring trajectories are generated by adding a Gaussian function term to the optimum trajectory, which is given as

$$q_{\text{neighboring}} = q_{\text{optimum}} \pm \varepsilon e^{-\frac{1}{2} \left( \frac{(t-\mu)^2}{\sigma^2} \right)}. \quad (21)$$

With  $\mu = 1$ ,  $\sigma = \mu/3$ , and  $\varepsilon = 0.2 \max(|q|)$ . Parameters for the Gaussian function are chosen so that the neighboring trajectories satisfy the boundary conditions for the optimal trajectory with negligible error. Fig. 11 shows the neighboring trajectories

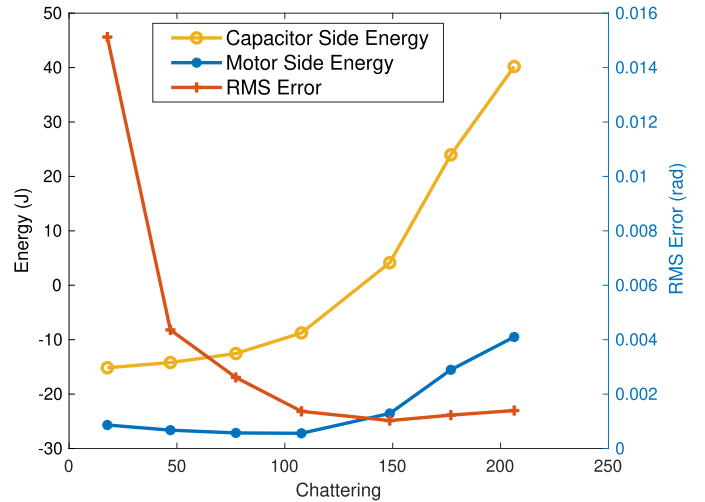


Fig. 12. Effect of chattering on energy regeneration.

followed by the robot and Table IV compares energy consumptions for the optimum and neighboring trajectories. We see that compared to the neighboring trajectories, the optimum trajectory results in the maximum total energy regeneration, even though Joint 3 consumes slightly more energy.

### C. Effect of Chattering

While conducting experiments, we observed that controller chattering had a negative effect on regeneration efficiency. Increasing the gains of the robust passivity based controller leads to lower tracking error of the optimum trajectories, but at a cost of increasing control signal chattering, which in turn reduces regeneration efficiency. This is demonstrated in Fig. 12, where we have increasing gains of the robust controller while following the A to B portion of the optimum trajectory in Case 1. Chattering is quantified empirically by summing the magnitude of the fast Fourier transform of the control signal between 10 Hz and the Nyquist frequency (500 Hz, one-half of the sampling rate) [40]. Fig. 12 shows that as the root-mean-square tracking error decreases, controller chattering increases. This initially results in a slight increase in energy regeneration (decrease in energy consumption) on the motor side, which can be related to more accurately tracking the optimal trajectory, but significantly decreases energy regeneration on the capacitor side, as a result of decrease in motor driver efficiency. After a certain point, increase in chattering significantly decrease energy regeneration on both motor and capacitor sides of the motor driver. Therefore, there is a compromise between how well the optimal trajectories are followed, and control signal chattering, and in certain cases it is necessary to give up trajectory tracking for more energy regeneration.

## VII. CONCLUSION

In this paper, we investigated robotic systems having ultracapacitor-based energy regenerative drive systems. For this purpose, a previously introduced framework was used to model the robot with the regenerative drive systems. Based on this

model an optimization problem is formulated to find point-to-point trajectories maximizing energy regeneration. The PUMA 500 robot is used as a case study. The problem was solved numerically and the optimal trajectories were implemented using a robust passivity based controller. Power flows are reported for the motor side and capacitor side of the motor driver. Experimental results show a good agreement with the theoretical results for the motor side of the motor driver and less agreement with the capacitor side. This is due to the efficiency of the motor driver and the power required to operate it. In addition, due to the fact that there was no energy entering the system from an external source [i.e.  $W_{\text{ext}} = 0$  and  $W_{\text{act}} = 0$  in (12)], energy is stored in the capacitor due to changes in mechanical energy, potential energy being the main contributor. This justifies the consideration of only the three main joints of the Puma 500 robot, which have potential for energy regeneration—compared to the three main joints; the robot wrist is lightweight, has significant friction, and moves slowly. Also, while conducting the experiments, it was observed that controller chattering has a negative effect on energy regeneration. In certain cases it might be necessary to compromise trajectory tracking for more energy regeneration. Using a higher quality motor driver can also mitigate the problems associated with motor driver. On the other hand, including the inefficiencies of the motor driver in the model could provide more energy regeneration by prompting the optimization to look for different trajectories that operate in the efficient range for the motor drivers. Results also showed that a great portion of the energy is dissipated as mechanical losses due to the robots design. Even with these losses, energy regeneration resulted in about 10–22% reduction in the overall energy consumption relative to the optimal regenerative trajectories. A comparison with trajectories re-optimized without regeneration yielded savings, which were slightly smaller but still significant.

In a factory assembly line with many robots, energy regeneration can lead to significant reduction in operating costs. As part of future research paths, an alternative approach to the one taken here could be to use model predictive control methods to provide optimal feedback directly, as opposed to solving for the optimal trajectory separately and enforcing it via a robust control method. Such an approach eliminates the need to reoptimize with changes in initial or final positions. Model predictive control involves a moving-horizon implementation of essentially the same optimal control solutions of this paper. The energy-based cost function, however, is not positive-definite relative to any particular equilibrium point, and the required feasibility, stability, and performance analyses fall into the category of *economic model predictive control* [58]. In addition, we only consider the star configuration for the semiactive joints. Using different configurations may lead to better results. This remains to be investigated in future work.

## APPENDIX A PUMA 500 ROBOT MODEL

The  $3 \times 10$  regressor matrix for the three main joints of the PUMA 500 robot (excluding the robot wrist) is given below where  $Y_{ij}$  is the  $i$ th row and  $j$ th column element of the regressor

matrix,  $c_i = \cos(q_i)$ ,  $s_i = \sin q_i$ ,  $c_{ij} = \cos(q_i + q_j)$ , and  $s_{ij} = \sin(q_i + q_j)$ .

$$\begin{aligned}
 Y_{11} &= \ddot{q}_1 \\
 Y_{12} &= \ddot{q}_1 c_2^2 - 2\dot{q}_1 \dot{q}_2 c_2 s_2 \\
 Y_{13} &= \ddot{q}_1 c_{23}^2 - 2\dot{q}_1 (\dot{q}_2 + \dot{q}_3) s_{23} c_{23} \\
 Y_{14} &= 2(\ddot{q}_1 - \dot{q}_1 \dot{q}_2) c_{23} c_2 - 2(\dot{q}_1 \dot{q}_2 + \dot{q}_1 \dot{q}_3) s_{23} c_2 \\
 Y_{15} &= (\dot{q}_2 + \dot{q}_3)^2 c_{23} + (\ddot{q}_2 + \ddot{q}_3) s_{23} \\
 Y_{16} &= Y_{17} = Y_{19} = Y_{110} = Y_{112} = Y_{113} = 0 \\
 Y_{18} &= \ddot{q}_2^2 c_2 + \ddot{q}_2 s_2, \quad Y_{22} = \ddot{q}_1^2 c_2 s_2, \quad Y_{23} = \ddot{q}_1^2 c_{23} s_{23} \\
 Y_{21} &= Y_{211} = Y_{213} = 0 \\
 Y_{24} &= (c_{23} s_2 + s_{23} c_2) \dot{q}_1^2 - (2\dot{q}_3 \dot{q}_2 + \dot{q}_3^2) s_3 \\
 &\quad + (2\ddot{q}_2 + \ddot{q}_3) c_3 \\
 Y_{25} &= \ddot{q}_1 s_{23}, \quad Y_{26} = \ddot{q}_2, \quad Y_{27} = \ddot{q}_3, \quad Y_{28} = \ddot{q}_1 s_2 \\
 Y_{29} &= -c_{23}, \quad Y_{210} = -c_2 \\
 Y_{31} &= Y_{32} = Y_{36} = Y_{38} = Y_{310} = Y_{311} = Y_{312} = 0 \\
 Y_{33} &= \dot{q}_1^2 s_{23} c_{23} \\
 Y_{34} &= \dot{q}_1^2 s_{23} c_2 + \dot{q}_2^2 s_3 + \ddot{q}_2 c_3 \\
 Y_{35} &= \ddot{q}_1 s_{23} \\
 Y_{37} &= \ddot{q}_2 + \ddot{q}_3 \\
 Y_{39} &= -c_{23}.
 \end{aligned}$$

The  $10 \times 1$  parameter vector,  $\theta$ , is given below where  $M_i$  is the mass of the  $i$ th robot link,  $I_{ij}$  is the moment of inertia of the  $i$ th link with respect to the  $j$  axis of the a coordinate frame located at the center of mass of link  $i$  and parallel to frame  $i$ ,  $C_{ij}$  is the distance from the center of mass of link  $i$ , along the  $j$  axis of frame  $i$ , to the origin of frame  $i$ , and  $g$  is the gravity constant. Refer to Figs. 3 and 4 for the definitions of the coordinate frames and other parameters. Numerical values identified for the parameter vector are also given as

$$\begin{aligned}
 \theta_1 &= M_2 d_2^2 + M_3 (d_3 - d_2)^2 + I_{1y} + I_{2x} + I_{3x} + m_1 n_1^2 \\
 &= 3.4677 \text{ kgm}^2 \\
 \theta_2 &= M_2 (C_{2x} + A_2)^2 + M_3 A_2^2 - I_{2x} + I_{2y} \\
 &= 0.9129 \text{ kgm}^2 \\
 \theta_3 &= M_3 C_{3x}^2 - I_{3x} + I_{3y} = 0.2377 \text{ kgm}^2 \\
 \theta_4 &= C_{3x} A_2 M_3 = 0.4387 \text{ kgm}^2 \\
 \theta_5 &= C_{3x} M_3 (d_3 - d_2) = -0.1525 \text{ kgm}^2 \\
 \theta_6 &= M_2 (C_{2x} + A_2)^2 + M_3 (C_{3x}^2 + A_2^2) + I_{2z} + I_{3z} + m_2 n_2^2 \\
 &= 4.2051 \text{ kgm}^2 \\
 \theta_7 &= I_{3z} + M_3 C_{3x}^2 + m_3 n_3^2 = 0.9622 \text{ kgm}^2
 \end{aligned}$$

TABLE V  
MEASURED VALUES FOR  $R$  AND  $a$

	$R$ ( $\Omega$ )	$a$ (Nm/A)
Joint 1	2.52	13.96
Joint 2	2.71	22.57
Joint 3	2.19	12.36

$$\begin{aligned}\theta_8 &= -d_2 M_2 (\mathcal{C}_{2x} + A_2) + A_2 M_3 (d_3 - d_2) \\ &= -0.8711 \text{ kgm}^2 \\ \theta_9 &= \mathcal{C}_{3x} g M_3 = 9.9665 \text{ Nm} \\ \theta_{10} &= g M_2 (\mathcal{C}_{2x} + A_2) + A_2 g M_3 = 42.1485 \text{ Nm.}\end{aligned}$$

$\mathcal{R}$  consists of the back EMF damping term ( $a^2/R$ ) and the combined nonlinear friction and damping effects of the robot joints and drive mechanism. The friction model used is taken from [59] and simplified by neglecting the Stribeck effects according to the work in [60]. For the  $j$ th link

$$\mathcal{R}_j = \frac{a_j^2}{R_j} \dot{q}_j + \gamma_{j1} \tanh(\gamma_{j2} \dot{q}_j) + \gamma_{j3} \tanh(\gamma_{j4} \dot{q}_j) + \gamma_{j5} \dot{q}_j \quad (22)$$

where  $\gamma$ s are constants of the friction model.

*Parameter identification:* Link length values,  $A_2$ ,  $d_2$ , and  $d_3$  are taken from [61] and verified by measuring the robot. The motor resistances  $R_j$  and the parameter  $a_j = \alpha_j n_j$  are derived from rearranging the electrical side equation for the regenerative drive (8) as

$$a_j \dot{q}_j - R_j \frac{i_j}{r_j} = r_j V_{\text{cap}} \quad (23)$$

and finding the least square solution by applying various trajectories for  $r_j$  and measuring the resulting  $\dot{q}_j$ ,  $i_j$ , and  $V_{\text{cap}}$ . Table V lists these values.

All other system parameters are found by solving a constrained optimization scheme based on (15), where the robot follows specially-constructed trajectories ( $q^e$ ,  $\dot{q}^e$ ,  $\ddot{q}^e$ ). System parameters are found that minimize the root mean squared error (RSME) of the measured virtual control ( $\tau_{\text{exp}}^d$ ) and the virtual control derived from (15) ( $\tau_{\text{model}}^d$ ).

$$\min_{\text{System Parameters}} \text{RSME}(\tau_{\text{exp}}^d - \tau_{\text{model}}^d)$$

$$\text{Lower Bound} \leq \text{System Parameters} \leq \text{Upper Bound} \quad (24)$$

To facilitate the numerical optimization, excitation trajectories are found by solving a separate optimization problem similar to what was done in [60]. The trajectories of the  $j$ th joint are represented as a finite Fourier series

$$\begin{aligned}q_j(t) &= \sum_{i=1}^N \frac{\mathcal{A}_i}{\omega_{fi}} \sin(\omega_{fi} t) - \frac{\mathcal{B}_i}{\omega_{fi}} \cos(\omega_{fi} t) \\ \dot{q}_j(t) &= \sum_{i=1}^N \mathcal{A}_i \cos(\omega_{fi} t) + \mathcal{B}_i \sin(\omega_{fi} t)\end{aligned}$$

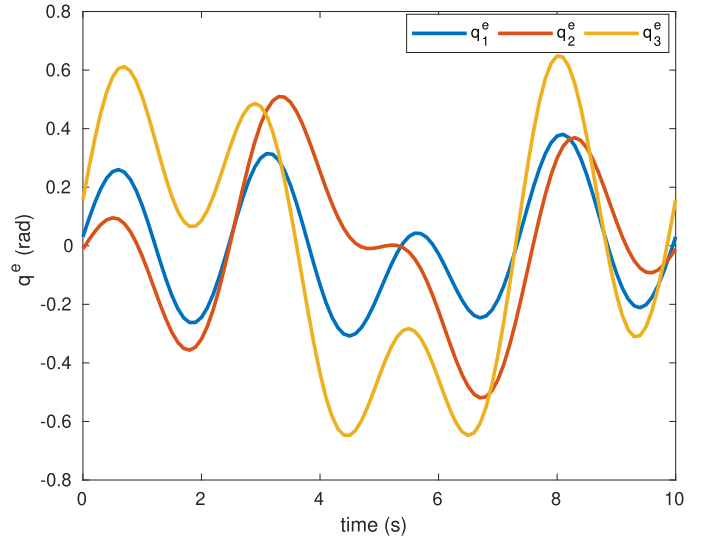


Fig. 13. Excitation trajectories found for the purpose of parameter identification.

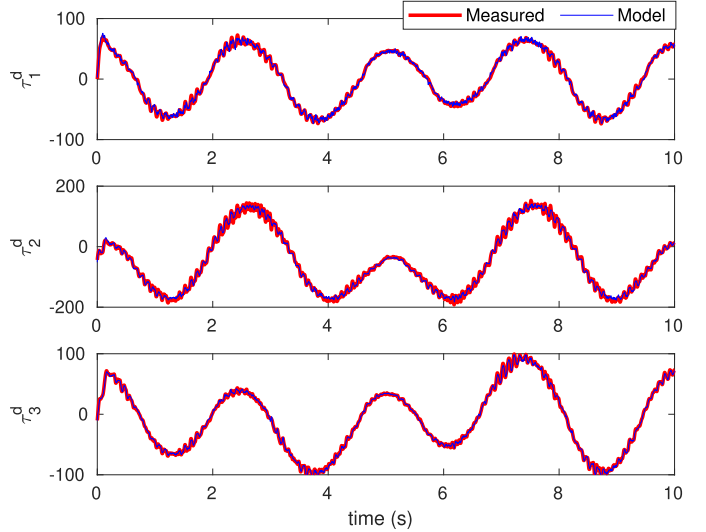


Fig. 14. Comparison of the measured ( $\tau_{\text{exp}}^d$ ) and modeled ( $\tau_{\text{model}}^d$ ) virtual control post optimization.

$$\dot{q}_j(t) = \sum_{i=1}^N -\mathcal{A}_i \omega_{fi} \sin(\omega_{fi} t) + \mathcal{B}_i \omega_{fi} \cos(\omega_{fi} t) \quad (25)$$

where  $\omega_f$  is the fundamental frequency. The Fourier series coefficients  $\mathcal{A}_i$  and  $\mathcal{B}_i$  are found by minimizing the condition number ( $\text{cond}()$ ) and maximizing the minimum singular value ( $\sigma_p()$ ) of the regressor matrix  $Y$

$$\begin{aligned}\min_{q, \dot{q}, \ddot{q}} \lambda_1 \text{cond}(Y) + \lambda_2 \frac{1}{\sigma_p(Y)} \\ \text{Lower Bound} \leq q, \dot{q}, \ddot{q} \leq \text{Upper Bound.} \quad (26)\end{aligned}$$

Excitation trajectories obtained in this manner will ensure minimum sensitivity to measurement noise and model uncertainty

TABLE VI  
 $\gamma$  VALUES IDENTIFIED FOR THE FRICTION MODEL

	$\gamma_1$	$\gamma_2$	$\gamma_3$	$\gamma_4$	$\gamma_5$
Joint 1	3.25	32.64	4.06	734.85	2.13
Joint 2	5.92	92.32	0	267.14	13.26
Joint 3	1.46	189.26	2.80	11.94	0.86

when obtaining system parameters [60]. For identifying the parameters of the Puma robot, we select  $N = 4$  and  $\omega_f = 2\pi/10$ . Fig. 13 shows the resulting excitation trajectories. After finding suitable excitation trajectories, the robot is made to follow these trajectories by using the robust passivity based control method. The optimization problem defined in (24) is then solved to identify system parameters. Fig. 14 compares the virtual control resulting from the optimized model ( $\tau_{\text{model}}^d$ ) and the virtual control measured from the Puma Robot ( $\tau_{\text{exp}}^d$ ). The resulting values for the parameter vector are given above, and the coefficients of the friction model are given in Table VI.

#### ACKNOWLEDGMENT

The authors would like to thank R. Harsha for his help in conducting the experiments and F. Rohani for his support in coding.

#### REFERENCES

- [1] S. M. Lukic, S. G. Wirasingha, F. Rodriguez, J. Cao, and A. Emadi, "Power management of an ultracapacitor/battery hybrid energy storage system in an HEV," in *Proc. IEEE Veh. Power Propulsion Conf.*, 2006, pp. 1–6.
- [2] P. Khalaf, H. Warner, E. Hardin, H. Richter, and D. Simon, "Development and experimental validation of an energy regenerative prosthetic knee controller and prototype," in *Proc. ASME Dyn. Syst. Control Conf.*, 2018, Art. no. V001T07A008.
- [3] J. Hitt, T. Sugar, M. Holgate, R. Bellman, and K. Hollander, "Robotic transtibial prosthesis with biomechanical energy regeneration," *Ind. Robot. Int. J.*, vol. 36, no. 5, pp. 441–447, 2009.
- [4] T. Shimizu and C. Underwood, "Super-capacitor energy storage for micro-satellites: Feasibility and potential mission applications," *Acta Astronaut.*, vol. 85, pp. 138–154, 2013.
- [5] H. Richter, "A framework for control of robots with energy regeneration," *J. Dyn. Syst., Meas., Control*, vol. 137, no. 9, 2015, Art. no. 091004.
- [6] B. E. Conway, *Electrochemical Supercapacitors: Scientific Fundamentals and Technological Applications*. Berlin, Germany: Springer, 2013.
- [7] A. Khaligh and Z. Li, "Battery, ultracapacitor, fuel cell, and hybrid energy storage systems for electric, hybrid electric, fuel cell, and plug-in hybrid electric vehicles: State of the art," *IEEE Trans. Veh. Technol.*, vol. 59, no. 6, pp. 2806–2814, Jul. 2010.
- [8] F. Khoshnoud *et al.*, "Energy regeneration from suspension dynamic modes and self-powered actuation," *IEEE/ASME Trans. Mechatronics*, vol. 20, no. 5, pp. 2513–2524, Oct. 2015.
- [9] E. Vinot and R. Trigu, "Optimal energy management of HEVs with hybrid storage system," *Energy Convers. Manage.*, vol. 76, pp. 437–452, 2013.
- [10] Z. Song, H. Hofmann, J. Li, J. Hou, X. Han, and M. Ouyang, "Energy management strategies comparison for electric vehicles with hybrid energy storage system," *Appl. Energy*, vol. 134, pp. 321–331, 2014.
- [11] A. Rufer and P. Barrade, "A supercapacitor-based energy-storage system for elevators with soft commutated interface," *IEEE Trans. Ind. Appl.*, vol. 38, no. 5, pp. 1151–1159, Sep./Oct. 2002.
- [12] Z. Zhang *et al.*, "A high-efficiency energy regenerative shock absorber using supercapacitors for renewable energy applications in range extended electric vehicle," *Appl. Energy*, vol. 178, pp. 177–188, 2016.
- [13] P. J. Grbovic, P. Delarue, P. Le Moigne, and P. Bartholomeus, "Modeling and control of the ultracapacitor-based regenerative controlled electric drives," *IEEE Trans. Ind. Electron.*, vol. 58, no. 8, pp. 3471–3484, Aug. 2011.
- [14] P. J. Grbovic, P. Delarue, P. Le Moigne, and P. Bartholomeus, "The ultracapacitor-based controlled electric drives with braking and ride-through capability: Overview and analysis," *IEEE Trans. Ind. Electron.*, vol. 58, no. 3, pp. 925–936, Mar. 2011.
- [15] A. S. Kammer and N. Olgac, "Enhancing energy harvesting capacity using delayed feedback control," in *Proc. IEEE Amer. Control Conf.*, 2016, pp. 1863–1868.
- [16] T. Asai and J. Scruggs, "Nonlinear stochastic control of self-powered variable-damping vibration control systems," in *Proc. IEEE Amer. Control Conf.*, 2016, pp. 442–448.
- [17] G. Carabin, E. Wehrle, and R. Vidoni, "A review on energy-saving optimization methods for robotic and automatic systems," *Robotics*, vol. 6, no. 4, 2017, Art. no. 39.
- [18] T. Izumi, P. Boyagoda, M. Nakaoka, and E. Hiraki, "Optimal control of a servo system regenerating conservative energy to a condenser," in *Proc. Int. IEEE/IAS Conf. Ind. Automat. Control, Emerg. Technol.*, 1995, pp. 651–656.
- [19] T. Izumi, "Energy saving manipulator by regenerating conservative energy," in *Proc. 6th IEEE Int. Workshop Adv. Motion Control*, 2000, pp. 630–635.
- [20] Y. Fujimoto, "Minimum energy biped running gait and development of energy regeneration leg," in *Proc. 8th IEEE Int. Workshop Adv. Motion Control*, 2004, pp. 415–420.
- [21] W. Xi, Y. Yesilevskiy, and C. D. Remy, "Selecting gaits for economical locomotion of legged robots," *Int. J. Robot. Res.*, vol. 35, no. 9, pp. 1140–1154, 2016.
- [22] S. Ha, S. Coros, A. Alspach, J. Kim, and K. Yamane, "Joint optimization of robot design and motion parameters using the implicit function theorem," presented at the Robot., Sci. Syst., 2017, doi: [10.15607/RSS.2017.XIII.003](https://doi.org/10.15607/RSS.2017.XIII.003).
- [23] G. Buondonno, J. Carpenter, G. Saurel, N. Mansard, A. De Luca, and J.-P. Laumond, "Actuator design of compliant walkers via optimal control," in *Proc. IEEE/RSJ Int. Conf. Intell. Robots Syst.*, 2017, pp. 705–711.
- [24] C. Hansen, J. Öltjen, D. Meike, and T. Ortmaier, "Enhanced approach for energy-efficient trajectory generation of industrial robots," in *Proc. IEEE Int. Conf. Automat. Sci. Eng.*, 2012, pp. 1–7.
- [25] B. L. Hunter, "Design of a self-contained, active, regenerative computer controlled above-knee prosthesis," Ph.D. dissertation, Dept. Mech. Eng., MIT Press, Cambridge, MA, USA, 1981.
- [26] B. Seth, "Energy regeneration and its application to active above-knee prostheses," Ph.D. dissertation, Dept. Mech. Eng., MIT Press, Cambridge, MA, USA, 1987.
- [27] K. A. Tabor, "The real-time digital control of a regenerative above-knee prosthesis," Ph.D. dissertation, Dept. Mech. Eng., MIT Press, Cambridge, MA, USA, 1988.
- [28] J. K. Hitt, T. G. Sugar, M. Holgate, and R. Bellman, "An active foot-ankle prosthesis with biomechanical energy regeneration," *J. Med. Devices*, vol. 4, no. 1, 2010, Art. no. 011003.
- [29] J. K. Hitt, R. Bellman, M. Holgate, T. G. Sugar, and K. W. Hollander, "The sparky (spring ankle with regenerative kinetics) project: Design and analysis of a robotic transtibial prosthesis with regenerative kinetics," in *Proc. ASME Int. Des. Eng. Tech. Conf. Comput. Inf. Eng. Conf.*, 2007, pp. 1587–1596.
- [30] M. A. Holgate, J. K. Hitt, R. D. Bellman, T. G. Sugar, and K. W. Hollander, "The sparky (spring ankle with regenerative kinetics) project: Choosing a dc motor based actuation method," in *Proc. 2nd IEEE RAS EMBS Int. Conf. Biomed. Robot. Biomechatronics*, 2008, pp. 163–168.
- [31] C. Everarts, B. Dehez, and R. Ronse, "Variable stiffness actuator applied to an active ankle prosthesis: Principle, energy-efficiency, and control," in *Proc. IEEE/RSJ Int. Conf. Intell. Robots Syst.*, 2012, pp. 323–328.
- [32] M. R. Tucker and K. B. Fite, "Mechanical damping with electrical regeneration for a powered transfemoral prosthesis," in *Proc. IEEE/ASME Int. Conf. Adv. Intell. Mechatronics*, 2010, pp. 13–18.
- [33] H. E. Warner, "Optimal design and control of a lower-limb prosthesis with energy regeneration," Master's thesis, Dept. Mech. Eng., Cleveland State Univ., Cleveland, OH, USA, 2015.
- [34] H. Warner, D. Simon, and H. Richter, "Design optimization and control of a crank-slider actuator for a lower-limb prosthesis with energy regeneration," in *Proc. IEEE Int. Conf. Adv. Intell. Mechatronics*, 2016, pp. 1430–1435.
- [35] R. Barick, H. Richter, A. van den Bogert, D. Simon, H. Warner, and T. Barto, "Optimal design of a transfemoral prosthesis with energy storage and regeneration," in *Proc. IEEE Amer. Control Conf.*, 2014, pp. 4108–4113.

- [36] F. Rohani, H. Richter, and A. J. Van den Bogert, "Optimal design and control of an electromechanical transfemoral prosthesis with energy regeneration," *PloS One*, vol. 12, no. 11, 2017, Art. no. e0188266.
- [37] A. Ghorbanpour and H. Richter, "Control with optimal energy regeneration in robot manipulators driven by brushless dc motors," in *Proc. ASME Dyn. Syst. Control Conf.*, 2018, Art. no. V001T04A003.
- [38] E. G. dos Santos and H. Richter, "Modeling and control of a novel variable-stiffness regenerative actuator," in *Proc. ASME Dyn. Syst. Control Conf.*, 2018, Art. no. V002T24A003.
- [39] H. De Las Casas, H. Richter, and A. Van Den Bogert, "Design and hybrid impedance control of a powered rowing machine," in *Proc. ASME Dyn. Syst. Control Conf.*, 2017, Art. no. V001T38A002.
- [40] H. Richter, X. Hui, A. van den Bogert, and D. Simon, "Semiactive virtual control of a hydraulic prosthetic knee," in *Proc. IEEE Conf. Control Appl.*, 2016, pp. 422–429.
- [41] P. Khalaf and H. Richter, "On global, closed-form solutions to parametric optimization problems for robots with energy regeneration," *J. Dyn. Syst., Meas., Control*, vol. 140, no. 3, 2018, Art. no. 031003.
- [42] P. Khalaf and H. Richter, "Parametric optimization of stored energy in robots with regenerative drive systems," in *Proc. IEEE Int. Conf. Adv. Intell. Mechatronics*, 2016, pp. 1424–1429.
- [43] O. von Stryk, "Numerical solution of optimal control problems by direct collocation," in *Optimal Control* (International Series of Numerical Mathematics), vol. 111, R. Bulirsch, A. Miele, J. Stoer, and K. Well, Eds. Basel, Switzerland: Birkhäuser, 1993.
- [44] H. Richter, D. Simon, and A. van den Bogert, "Semiactive virtual control method for robots with regenerative energy-storing joints," in *Proc. 19th IFAC World Congr.*, 2014, pp. 10244–10250.
- [45] M. Spong, S. Hutchinson, and M. Vidyasagar, *Robot Modeling and Control*. Hoboken, NJ, USA: Wiley, 2006.
- [46] D. C. Karnopp, D. L. Margolis, and R. C. Rosenberg, *System Dynamics: Modeling, Simulation, and Control of Mechatronic Systems*. Hoboken, NJ, USA: Wiley, 2012.
- [47] P. J. Grbovic, *Ultra-Capacitors in Power Conversion Systems: Analysis, Modeling and Design in Theory and Practice*. Hoboken, NJ, USA: Wiley, 2013.
- [48] S. Buller, E. Karden, D. Kok, and R. De Doncker, "Modeling the dynamic behavior of supercapacitors using impedance spectroscopy," in *Proc. 36th IEEE/IAS Annu. Meet. Conf. Rec. Ind. Appl. Conf.*, 2001, vol. 4, pp. 2500–2504.
- [49] C.-J. Chiang, J.-L. Yang, and W.-C. Cheng, "Dynamic modeling of the electrical and thermal behavior of ultracapacitors," in *Proc. 10th IEEE Int. Conf. Control Autom.*, 2013, pp. 1839–1844.
- [50] N. Bertrand, J. Sabatier, O. Briat, and J.-M. Vinassa, "Fractional non-linear modelling of ultracapacitors," *Commun. Nonlinear Sci. Numer. Simul.*, vol. 15, no. 5, pp. 1327–1337, 2010.
- [51] P. Khalaf, "Design, control and optimization of robots with advanced energy-regenerative drive systems," Ph.D. dissertation, Dept. Mech. Eng., Cleveland State University, Cleveland, OH, USA, 2019. [http://frave.ohiolink.edu/etdc/view?acc\\_num=csu1552923998768344](http://frave.ohiolink.edu/etdc/view?acc_num=csu1552923998768344)
- [52] D. E. Kirk, *Optimal Control Theory: An Introduction*. Chelmsford, MA, USA: Courier Corporation, 2012.
- [53] A. J. Van Den Bogert, D. Blana, and D. Heinrich, "Implicit methods for efficient musculoskeletal simulation and optimal control," *Proc. IUTAM*, vol. 2, pp. 297–316, 2011.
- [54] Control, Robotics and Mechatronics Lab, *Code for Energy Regeneration Optimization*. 2018. Accessed: Dec. 11, 2018. [Online]. Available: <https://github.com/csurowing/regenrobotics/blob/master/DCoptPuma>
- [55] A. Wächter and L. T. Biegler, "On the implementation of an interior-point filter line-search algorithm for large-scale nonlinear programming," *Math. Program.*, vol. 106, no. 1, pp. 25–57, 2006.
- [56] Control, Robotics and Mechatronics lab, *Video of Puma Robot Following Optimized Trajectories for Each Studied Case*. 2018. Accessed: Dec. 11, 2018. [Online]. Available: <https://www.youtube.com/channel/UCExuudaRqwM3KQjxIalQFvQ>, 2018
- [57] V. Musolino, L. Piegaro, and E. Tironi, "New full-frequency-range supercapacitor model with easy identification procedure," *IEEE Trans. Ind. Electron.*, vol. 60, no. 1, pp. 112–120, Jan. 2013.
- [58] M. A. Müller and F. Allgöwer, "Economic and distributed model predictive control: Recent developments in optimization-based control," *SICE J. Control, Meas., Syst. Integr.*, vol. 10, no. 2, pp. 39–52, 2017.
- [59] C. Makkar, W. Dixon, W. Sawyer, and G. Hu, "A new continuously differentiable friction model for control systems design," in *Proc. IEEE/ASME Int. Conf. Adv. Intell. Mechatronics*, 2005, pp. 600–605.
- [60] A. H. Memar and E. T. Esfahani, "Modeling and dynamic parameter identification of the SCHUNK powerball robotic arm," in *Proc. ASME Int. Des. Eng. Tech. Conf. Comput. Inf. Eng. Conf., and the 39th Mechanisms Robot. Conf.*, 2015, vol. 5C, Art. no. V05CT08A024.
- [61] P. I. Corke and B. Armstrong-Helouvry, "A search for consensus among model parameters reported for the PUMA 560 robot," in *Proc. IEEE Int. Conf. Robot. Automat.*, 1994, pp. 1608–1613.



**Poya Khalaf** received the M.Sc. degree in mechanical engineering from the Iran University of Science and Technology, Tehran, Iran, in 2012. He is currently working toward the Ph.D. degree in mechanical engineering from Cleveland State University, Cleveland, OH, USA.

His current research interests include modeling, design, and control of energy regenerative robotic systems, powered lower limb prosthesis, and minimally invasive robotic surgery.



**Hanz Richter** received the B.Sc. degree from Pontificia Universidad Católica del Perú, Lima, Peru, in 1995, the M.Sc. and Ph.D. degrees from the Oklahoma State University, Stillwater, OK, USA, in 1997 and 2001, respectively, all in mechanical engineering.

He is currently a Professor of Mechanical Engineering with Cleveland State University, Cleveland, OH, USA. His current research interests include the broad areas of control, robotics, and mechatronics with applications to biomedical robotics, aerospace propulsion, high-precision motion control and smart sensors. His research funding has been supported by the U.S. National Science Foundation, NASA, the State of Ohio, the Parker–Hannifin Corporation and the Cleveland Clinic Foundation.